X-ray line polarization of He-like Si satellite spectra in plasmas driven by high-intensity ultrashort pulsed lasers

Peter Hakel* and Roberto C. Mancini
Department of Physics, University of Nevada, Reno, Nevada 89557, USA

Jean-Claude Gauthier†
Laboratoire pour l'Utilisation des Lasers Intenses, CNRS UMR 7605, Ecole Polytechnique — CEA — Université Paris VI, 91128 Palaiseau, France

Emilio Mínguez
Instituto de Fusión Nuclear, Universidad Politécnica de Madrid, 28006 Madrid, Spain

Jacques Dubau and Marguerite Cornille
Observatoire de Paris, 92915 Meudon, France
(Received 16 June 2003; revised manuscript received 24 December 2003; published 18 May 2004)

We present a modeling study of x-ray line polarization in plasmas driven by high-intensity, ultrashort duration pulsed lasers. Electron kinetics simulations of these transient and nonequilibrium plasmas predict non-Maxwellian and anisotropic electron distribution functions. Under these conditions, the magnetic sublevels within fine structure levels can be unequally populated which leads to the emission of polarized lines. We have developed a time-dependent, collisional-radiative atomic kinetics model of magnetic sublevels to understand the underlying processes and mechanisms leading to the formation of polarized x-ray line emission in plasmas with anisotropic electron distribution functions. The electron distribution function consists of a thermal component extracted from hydrodynamic calculations and a beam component determined by PIC simulations of the laser-plasma interaction. We focus on the polarization properties of the He-like Si satellites of the Ly_α line, discuss the time evolution of polarized satellite spectra, and identify suitable polarization markers that are sensitive to the anisotropy of the electron distribution function and can be used for diagnostic applications.

DOI: 10.1103/PhysRevE.69.056405 PACS number(s): 52.38.Ph, 32.30.Rj

I. INTRODUCTION

In the last decade, polarized x-ray line emissions have attracted attention as spectral signatures of anisotropy in hot plasmas. The existence of a special direction in space caused, for instance, by the presence of directional energetic electrons or electric and magnetic fields can lead to preferential (i.e., uneven) population of the magnetic sublevels associated with a fine structure energy level. This condition is called alignment. The degree of polarization is related to the quantitative characteristics of plasma anisotropy such as the energy and angular distribution of directional electrons. Polarization-based plasma spectroscopy has therefore been recognized as a potential diagnostic tool to characterize plasma anisotropy. An extensive review of previous work in this subject can be found in Refs. [1,2].

Fundamental quantum mechanical studies aimed at obtaining insights into the mechanism and characteristics of polarized line emissions have mostly been done using the density-matrix formalism [3–7]. The focus of such investigations has typically been on astrophysical plasmas, and on experiments such as the electron beam ion trap (EBIT) where well-controlled experimental conditions enable detailed testing of theories at the atomic physics level. In other publications [8,9] we presented an alternative method for the calculation of polarized x-ray line emissions based on the atomic kinetics modeling of magnetic sublevel populations and the subsequent use of multipole radiation field properties. We have benchmarked this method in the calculation of polarization-dependent spectra of dielectronic satellite line emissions in B- and Be-like Fe and He-like Si [4,10], and in the K-shell $1s2l \rightarrow 1s^2$ x-ray line spectra of He-like Fe, driven by a monoenergetic, unidirectional, and unpolarized electron beam [6]. The main highlight of this method is a straightforward account of many (competing) atomic processes by including in the atomic kinetics model all the relevant structures of energy levels and atomic rates connecting them. This feature makes the method attractive for plasma applications where the kinetics of level populations is usually determined as a result of the competition between several atomic processes, and it goes beyond previous analysis of polarized line emissions in plasmas based on the two-level atom approximation [1,11,12]. In particular, the effect of multilevel atomic kinetics was demonstrated in the case of He-like Fe lines in an EBIT environment, where cascades from $1s\ 3l$ levels affect the polarization of the $1s\ 2l \rightarrow 1s^2$ lines when $1s\ 3l$ levels are open for direct excitation from the ground state [8,13].

*Present address: Theoretical Division, Los Alamos National Laboratory, Los Alamos, New Mexico 87545, USA.

†Present address: CELIA, Université Boudeaux, F-33405 Talence Cedex, France.

TABLE I. $2l\ 2l' \rightarrow 1s\ 2l$ singlet and triplet transitions in He-like Si.

Label	Line transition	Photon energy (eV)
1	$2p^2 {}^1D_2 \rightarrow 1s\ 2p\ {}^1P_1$	1980
2	$2s\ 2p\ {}^1P_1 \rightarrow 1s\ 2s\ {}^1S_0$	1992
3	$2s\ 2p^3P_0 \rightarrow 1s\ 2s\ {}^3S_1$	1984
4	$2s\ 2p^3P_1 \rightarrow 1s\ 2s\ {}^3S_1$	1985
5	$2s\ 2p^3P_2 \rightarrow 1s\ 2s\ {}^3S_1$	1986
6	$2p^2\ {}^3P_1 \rightarrow 1s\ 2p\ {}^3P_0$	1984
7	$2p^2\ {}^3P_1 \rightarrow 1s\ 2p\ {}^3P_1$	1983
8	$2p^2\ {}^3P_1 \rightarrow 1s\ 2p^3P_2$	1982

Plasma spectroscopy diagnostics that have been successfully developed in connection with detailed multilevel atomic kinetics modeling have mainly relied on the properties of spectral line intensities and detailed line shape calculations to extract information about the state of the plasma. However, they do not provide information about plasma anisotropy. Here, we consider the problem of plasma anisotropy determination and present a model for the calculation of polarization-dependent x-ray line spectra in plasmas. We calculate the time histories of magnetic sublevel populations using a fundamental time-dependent collisional-radiative atomic kinetics model, and then we use these populations to compute polarized x-ray line intensities taking into account the characteristics of multipole radiation fields. In particular, we focus on the polarization properties of the He-like satellites of the Ly_α line in silicon plasmas produced by high-intensity ultrashort duration laser pulses. These satellite lines (see Table I) are usually observed on the low-energy side of the Ly_α line; they are typically emitted during a period of time that is short compared to that of the resonance line, and are optically thin. All these considerations can facilitate the interpretation of the recorded spectra. Furthermore, silicon has no nuclear magnetic dipole moment and thus no hyperfine interaction which, in turn, tends to destroy alignment in the atomic energy levels.

In an effort to perform a realistic modeling study of polarized x-ray line emission in a silicon laser-produced plasma, atomic kinetics and synthetic spectra calculations are done in combination with hydrodynamic simulations of the overall evolution of plasma conditions in the target. In addition, a particle-in-cell code is used to model the electron kinetics of the laser-plasma interaction and the production of alignment-creating directional electrons. Thus, the polarization-dependent spectrum results have built-in the effects of hydrodynamics, and electron and atomic kinetics. Furthermore, the magnetic sublevel atomic kinetics self-consistently includes the effects of alignment-creating atomic processes driven by beamlike electrons as well as alignment-destroying atomic processes driven by thermal (Maxwellian) electrons, and hence the polarization effect on the x-ray lines can be studied over a range of plasma conditions where different effects become dominant at different times. We analyze and determine the importance of various atomic processes and their impact on observable polarization-dependent spectral features, and we also discuss the dependence of line emission characteristics on the properties of the driving laser.

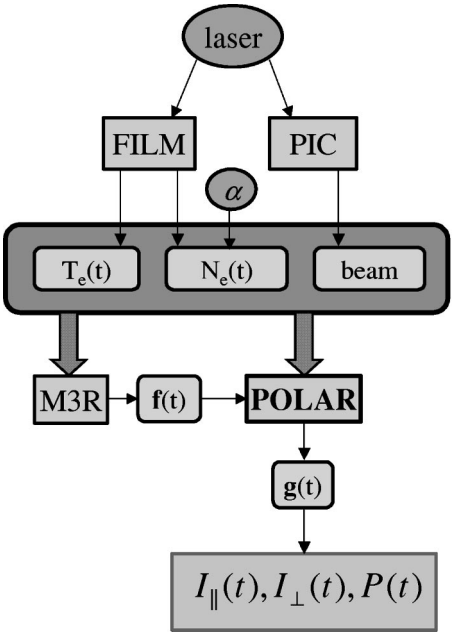

FIG. 1. Schematic illustration of the suite of codes used in the model calculations (see discussion in the main text). The vectors $\boldsymbol{f}(t)$ and $\boldsymbol{g}(t)$ are the time histories of fractional populations computed by M3R and POLAR, respectively, α is an adjustable parameter that characterizes the fraction of beam electrons in the model, and $I_\parallel(t)$, $I_\perp(t)$, and $P(t)$ are the time histories of parallel and perpendicular intensities, and the degree of polarization, respectively.

This paper is organized as follows. In Sec. II we discuss the details of our modeling calculations including hydrodynamics, electron kinetics and, in particular, the time-dependent, collisional-radiative magnetic sublevel atomic kinetics model and the atomic databases used to calculate polarization-dependent spectra. In Sec. III we present results for the case of the He-like Si satellite line emission and identify polarization-sensitive lines that can be used as markers of anisotropy in the plasma, and in Sec. IV we present our conclusions.

II. MODEL

The goal of our model calculations is to investigate the formation of x-ray line polarization-dependent spectra in a plasma whose temperature, density, and anisotropy are rapidly evolving in time, and where alignment-creating and destroying processes compete to determine the population distribution of magnetic sublevels. This requires the consideration of plasma hydrodynamics, and electron and atomic kinetics. To this end, a suite of codes is run in succession according to the scheme shown in Fig. 1.

A. Hydrodynamics and electron kinetics

First, laser pulse and target parameters are used to run FILM. This is a one-dimensional (1D), two-temperature (i.e., electron and ion) Lagrangian hydrodynamics code that simu-

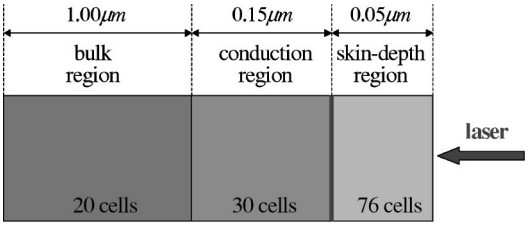

Fig. 2

FIG. 2. Target zones and discretization used in the FILM hydrodynamic simulation.

lates the overall target behavior as it is heated by the laser, including laser energy coupling and deposition, electron and ion heat conduction, and hydrodynamic motion [14]. The equation of state is taken from the Sesame EOS library [15]. For the simulations performed here, the silicon target is divided into a total of 126 fluid elements or cells (see Fig. 2) grouped in three main regions: (1) the outermost ("skin depth") region of thickness 0.05 μm where the laser energy is directly deposited is described with 76 cells, (2) the "conduction" region 0.15 μm thick, which is heated indirectly by heat conduction from the skin depth region, is modeled with 30 cells, and (3) a 1 μm "bulk" region which provides the boundary condition representing a target substrate is characterized by 20 cells. The code calculates various characteristics of each cell, including time histories of electron and total ion number densities (i.e., mass density), and electron temperature. These parameters are needed to drive the atomic kinetics codes M3R and POLAR, which compute ionization balance, magnetic sublevel populations, and polarization-dependent synthetic spectra. In these simulations, the P-polarized laser pulse had a Gaussian temporal profile centered at 400 fs and a FWHM of 300 fs, the wavelength was 800 nm, the incidence angle with respect to the normal of the target was 45°, and laser intensities were in the range from 2×10^{16} W cm^{-2} to 5×10^{17} W cm^{-2}. Typical FILM time histories for the electron number density $N_e(t)$ and temperature $T_e(t)$ characteristic of several fluid elements in the simulation are shown in Fig. 3. Early in time the electron number density rises driven by the rapid ionization of the plasma; then, the hydrodynamic decompression begins and the electron density drops at a slower rate. The electron temperature time history qualitatively follows the laser pulse time profile, peaking slightly after the peak of the laser pulse. Cells closer to the front surface go through time histories characteristic of higher temperatures and lower densities relative to those of cells deeper in the target. As the laser intensity increases maximum temperatures increase as well while their time profile remains qualitatively similar. On the other hand, maximum densities are similar in value but occur earlier in time, and are followed by a hydrodynamic decompression that proceeds at a faster rate which, in turn, results in lower values of the electron density at later times. Electron temperature and number density time histories are post-processed to calculate time-dependent ionization balance and magnetic sublevel populations with M3R and POLAR, respectively.

Plasma electrons can be characterized as thermal and nonthermal. On the one hand, nonthermal electrons can affect the overall ionization balance of the plasma and, if their distribution is anisotropic, they can also create alignment in the atomic energy levels which results in polarized line emissions. On the other hand, the thermal electrons destroy the alignment effect by their tendency to evenly populate the magnetic sublevels of a given fine structure energy level. In our model we account for both groups of electrons by splitting the electron pool of density N_e (calculated by FILM) into a thermal (Maxwellian) part of distribution $f_M(E,kT)$, density $(1-\alpha)N_e$, and temperature kT (calculated by FILM), and a beam part described by an energy distribution $f_B(E)$ and density αN_e. The fraction of directional, nonthermal electrons α is a constant free parameter in our model. We have tested several α values and found that they produce the expected rise of alignment and polarization effects in the line emission with increasing α, and vanishing polarization for $\alpha=0$. In this work we illustrate our results for the case $\alpha=0.2$ that has been chosen in accordance with previous estimates for the laser irradiation conditions assumed here [16]. The energy distribution $f_M(E,kT)$ of the thermal electrons is characterized by the electron temperature time history calcu-

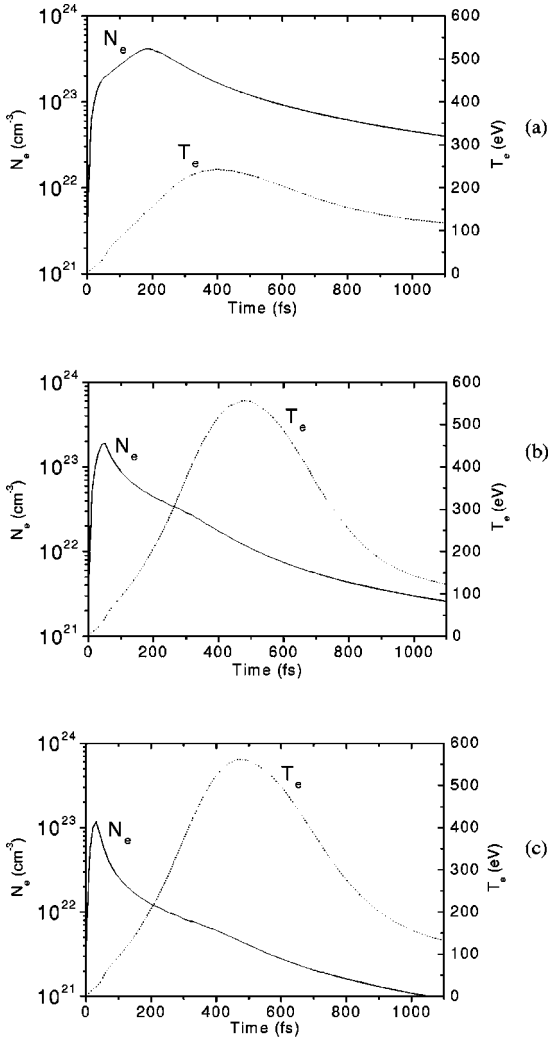

FIG. 3. Electron temperature $T_e(t)$ and number density $N_e(t)$ time histories calculated by FILM for a laser intensity of 2×10^{16} W cm^{-2}, and for cells deep in the target (a), close to the target's surface (b), and very close to the target's surface (c).

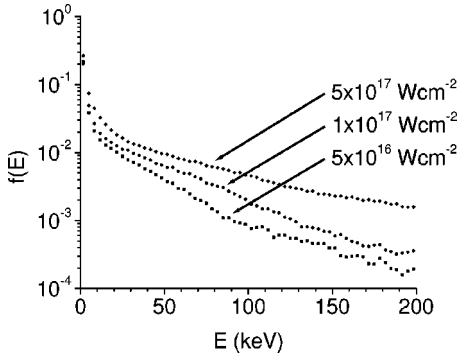

FIG. 4. Energy distribution of beamlike electrons calculated by EUTERPE for laser intensities of 5×10^{16} W cm^{-2}, 1×10^{17} W cm^{-2}, and 5×10^{17} W cm^{-2}.

lated by FILM. The energy distribution of the electron beam is obtained from the 1-1/2D particle-in-cell code EUTERPE that models the electron kinetics of the production of a beam of energetic electrons due to resonance absorption in the laser-plasma interaction [17]. This code calculates the motion of relativistic electrons and mobile ions (the mass ratio between electrons and ions is given by $m_i/Zm_e=3600$) in the field of a *P*-polarized, plane electromagnetic wave; the 45° incidence angle is treated by means of a relativistic boost-frame transformation. Figure 4 illustrates the energy distribution of the beamlike electrons computed by EUTERPE for several laser intensities at the end of the laser pulse. The code also calculates the family of time histories of the electron distribution functions that are then used to calculate collisional atomic rates associated with the beamlike electrons. The trend of these results is clear: the larger the laser intensity the more energetic electrons are produced. The electron beam is collimated along the normal to the surface of the target, which also defines the axis of quantization for this problem, and its energy distribution is normalized by the condition $\int_0^\infty f_B(E)dE=1$. In this model, EUTERPE simulations begin 100 fs into the FILM time evolution with an isotropic electron distribution function initially characterized by a 1D "temperature" of 0.6 keV [i.e., $f_B(E)\propto\exp(-E(\mathrm{keV})/0.6)$]. As time progresses, the beamlike distribution evolves, and a tail of energetic electrons develops in the distribution.

B. Magnetic sublevel atomic kinetics

Next, given the plasma electron characteristics obtained from FILM and EUTERPE, we calculate the overall ionization balance using the M3R code, and magnetic sublevel populations with POLAR. The M3R code implements a time-dependent collisional-radiative atomic kinetics model that we use to calculate the overall ionization of the silicon plasma, and the time histories of the level populations of ground and excited nonautoionizing states [18]. The energy level structure is described by 514 LS terms spread over all ionization stages from the Ne-like Si ion to the fully stripped Si ion. It uses an atomic database comprised of 21 643 absorption oscillator strengths calculated with Cowan's atomic structure code [19] which are used to calculate the rates associated with electron collisional excitation and deexcitation, and spontaneous radiative decay. Also, electron collisional ionization and recombination, and radiative and dielectronic recombination processes are included in M3R. In particular, M3R time histories of He- and H-like Si ground state populations serve as input for POLAR, a detailed time-dependent collisional-radiative magnetic-sublevel atomic kinetics code. In this way, the information about the evolution of the ionization balance in the silicon plasma is built-in into POLAR calculations. There are substantial transient effects in the ionization balance that become evident when comparing the results of M3R runs in steady-state and time-dependent modes. These differences are "inertia-type effects" in the level populations associated with the finite relaxation times of the atomic rates that, in the transient case, prevent the populations from instantaneously adjusting to rapidly changing plasma conditions (as it would be the case in a steady-state regime). Nonthermal effects are also included in the M3R calculation, and they are found to make a significant contribution towards driving the ionization balance faster and populating the He- and H-like ions.

The POLAR code implements a fundamental time-dependent collisional-radiative atomic kinetics model for calculating the time histories of magnetic sublevel populations and, subsequently, polarization-dependent line spectra. This is accomplished by setting up a system of collisional-radiative atomic kinetics rate equations for magnetic sublevels. For the cases considered here, this system of equations can be written in matrix notation as follows:

$$\frac{d\vec{g}}{dt}=\underline{\underline{A}}\vec{g}+\vec{b}, \tag{1}$$

where $\vec{g}$ is the vector of He-like Si magnetic-sublevel populations, $\underline{\underline{A}}$ is the rate matrix associated with the atomic processes included in the model, and $\vec{b}$ is a vector that takes into account population effects proportional to He- and H-like Si ground state populations. Implicit in the model is the axis of quantization with respect to which the magnetic sublevel quantum number M and the direction of observation are referred to, and axial symmetry is assumed; we take the z-coordinate axis to be this axis. Electron collisional rates are calculated using the electron distribution function discussed above. However, we emphasize that the electron distribution function is input to the model and thus other electron distribution functions could be considered as well. POLAR can be run either in the steady-state or the fully transient mode. With the magnetic sublevel populations from POLAR, we then calculate the time histories of polarization-dependent total line intensities $I_\parallel$ and $I_\perp$. $I_\parallel$ represents the intensity of radiation observed at a right angle with respect to the axis of quantization and linearly polarized along this axis. Analogously, $I_\perp$ is the intensity of radiation linearly polarized in a direction perpendicular to the quantization axis.

In general, to address the problem of calculating polarized line emission one has to consider the density matrix of the ion and electromagnetic field system. From here, the photon density matrix can be extracted which contains the Stokes parameters that characterize the polarization properties of the radiation field. The diagonal elements of the ion density ma-

TABLE II. Relative multipole intensities of electric ($E1$) and magnetic ($M1$) dipole transitions. θ and φ are the polar and azimuth angles of spherical coordinates, respectively. For $\theta=90°$ $\hat{\theta}$ defines the parallel and $\hat{\varphi}$ the perpendicular polarization states.

	$E1$		$M1$	
	MI_θ	MI_φ	MI_θ	MI_φ
$\Delta M=0$	$3\sin^2\theta$	0	0	$3\sin^2\theta$
$\Delta M=+/-1$	$(3/2)\cos^2\theta$	3/2	3/2	$(3/2)\cos^2\theta$

trix are the magnetic-sublevel populations, and the off-diagonal elements represent coherences. However, for the case of systems with axial symmetry the ion-density matrix remains diagonal and the line polarization properties are characterized only by magnetic-sublevel populations [5]. A line transition is formed as an incoherent collection of sublevel transitions that are inherently polarized as a result of angular momentum conservation of the ion and photon system. These sublevel transitions overlap due to energy degeneracy in upper and lower fine structure levels (i.e., J levels). Therefore, given the magnetic-sublevel populations and the properties of multipole radiation fields [20], optically thin polarization-dependent total line intensities $I_\parallel$ and $I_\perp$ can then be calculated as follows:

$$I_{\parallel,\perp} \propto h\nu \quad A(J_i \rightarrow J_f) \times \sum_{M_i=-J_i}^{J_i} f(M_i) \sum_{M_f=-J_f}^{J_f} MI_{\parallel,\perp}(\Delta M,$$

$$\theta = 90° \times \langle J_f \quad q \quad M_f \quad -\Delta M \,|J_i \quad M_i\rangle^2, \qquad (2)$$

where $h\nu$ is the transition energy, $A(J_i \rightarrow J_f)$ is the transition's radiative decay rate, $f(M_i)$ are populations of upper level's magnetic sublevels, q is the multipolarity of the transition, $\Delta M = M_f - M_i$, and $\langle|\rangle$ is a Clebsch-Gordan coefficient. The products of Clebsch-Gordan coefficients and $A(J_i - J_f)$ are the spontaneous radiative decay rates of the constituent magnetic-sublevel transitions [21]. The $MI(\Delta M, \theta)$'s are relative multipole intensities based on wave-zone multipole fields, in particular their angular parts that are also known as vector spherical harmonics [20], and θ is the angle between the direction of observation and the axis of symmetry. Their values for dipole and quadrupole transitions are listed in Tables II and III. Given $I_\parallel$ and $I_\perp$, the degree of polarization is calculated according to

$$P = \frac{I_\parallel - I_\perp}{I_\parallel + I_\perp}. \qquad (3)$$

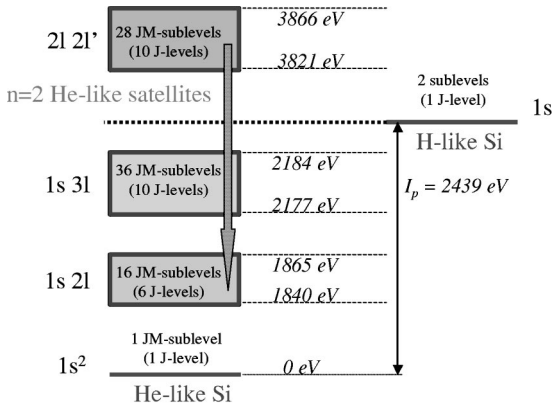

FIG. 5. Schematic illustration of the energy level structure included in POLAR for studying the polarization properties of the He-like satellites of the Ly_α line.

The implementation of POLAR for investigating the polarization of He-like satellite lines of the Ly_α in silicon includes the two magnetic sublevels of the ground state in H-like Si, and the 81 magnetic sublevels in He-like Si arising from the configurations $1s^2$, $1s\,2l$, $1s\,3l''$, and $2l\,2l'$ where l and l' can be s or p, and l'' can be s, p, or d (see Fig. 5). The $1s\,2l$ and $2l\,2l'$ states give rise to the upper and lower levels of the transitions of interest. As mentioned above, He- and H-like ion ground state population, time histories are taken from the M3R calculation, and then used in POLAR to compute the sublevel population time histories of singly and doubly excited states in He-like Si. We note that M3R does not calculate magnetic sublevel populations. However, the ground state of the He-like ion $1s^2\ {}^1S_0$ has only one magnetic sublevel and the two magnetic sublevels of the ground state of the H-like ion $1s\ {}^2S_{1/2}$ are always equally populated due to the axial symmetry assumption. Thus, magnetic sublevel populations for these ground states are readily obtained from those calculated by M3R. The following atomic processes are taken into account: electron capture from and autoionization to H-like $1s$, electron collisional excitation/deexcitation between $1s^2$, $1s\,2l$ and $1s\,3l$, inner-shell electron collisional excitation/deexcitation between $1s\,2l$ and $2l\,2l'$, and $1s^2$ and $2l\,2l'$ (which are more important than the collisional excitation from $1s\,3l$ to $2l\,2l'$), collisional mixing between $2l\,2l'$, and all possible electric-dipole ($E1$) spontaneous radiative decays between He-like levels. These atomic processes fall in two categories: isotropic and anisotropic, depending upon their intrinsic characteristics and/or whether they are driven by thermal or beam-type electrons. Isotropic processes include spontaneous radiative decay, autoionization decay, thermal-electron-driven electron capture, and col-

TABLE III. Same as in Table II but for electric ($E2$) and magnetic ($M2$) quadrupole transitions.

	$E2$		$M2$	
	MI_θ	MI_φ	MI_θ	MI_φ
$\Delta M=0$	$15\sin^2\theta\cos^2\theta$	0	0	$15\sin^2\theta\cos^2\theta$
$\Delta M=+/-1$	$(5/2)(2\cos^2\theta-1)^2$	$(5/2)\cos^2\theta$	$(5/2)\cos^2\theta$	$(5/2)(2\cos^2\theta-1)^2$
$\Delta M=+/-2$	$(5/2)\sin^2\theta\cos^2\theta$	$(5/2)\sin^2\theta$	$(5/2)\sin^2\theta$	$(5/2)\sin^2\theta\cos^2\theta$

lisional excitation and deexcitation. While these processes cannot create alignment, they are capable of transferring preexisting alignment from initial to final levels. The actual alignment creation occurs through anisotropic processes driven by beam-type electrons. Anisotropic processes considered in our model are electron collisional excitation and electron capture. These are the processes that can create the line polarization effect by preferential population of magnetic sublevels. Electron collisional deexcitation driven by energetic beam-type electrons is not included since this is a zero-threshold process and hence it is dominated by thermal electrons. Thermal electrons can also destroy alignment through elastic scattering by redistributing a fine-structure level's population equally among its sublevels. We emphasize that within the context of this model the polarization degree is the result of the competition between anisotropic (alignment-creating) and isotropic (alignment-destroying or transferring) atomic processes.

The atomic database for POLAR contains 1302 spontaneous radiative decay rates, 28 autoionization rates, and 2087 collisional excitation cross sections connecting magnetic sublevels. Energy levels and electric-dipole spontaneous radiative decay rates were calculated with the Los Alamos atomic structure code CATS [19,22]. Autoionization decay rates were calculated using the Los Alamos atomic ionization code GIPPER [23]. From these J-level autoionization rates, JM-sublevel autoionization and electron capture rates associated with the thermal- and beam-type electrons were calculated using the method described in Ref. [8]. Since there is little experience with the generation of large databases of sublevel cross sections, electron collisional excitation cross sections as functions of electron energy were obtained by two independent calculations and then checked against each other for consistency. First, the Los Alamos electron scattering code ACE [24] was used to generate a complete database of cross sections for this application in the Coulomb-Born approximation. Second, a portion of this database was independently calculated with the UCL/JAJOM codes [5,25] in the distorted-wave approximation including unitarization. Very good overall agreement was found between these two sets of sublevel cross sections. As an illustration, in Fig. 6 we show the collisional excitation cross section of $1s\ 2s\ ^1S_0,\ M=0 \rightarrow 2s\ 2p\ ^1P_1,\ M=0$ and ± 1 driven by an electron beam. In this example the agreement is particularly remarkable at lower electron energies (up to 10 keV or 1000 Ry) that are characteristic of most electrons in plasmas under consideration.

The UCL code also allows us to calculate data characterizing redistribution of population among the sublevels of a given J level due to elastic electron-ion scattering driven by thermal electrons. This process destroys alignment in any given J level and can therefore lead to the loss of polarization effect in line transitions originating from this J level. In our model the elastic scattering process is accounted for in $2s\ 2p\ ^1P_1$ and $2p^2\ ^1D_2$. Rates for thermal-electron-driven elastic scattering are calculated by integrating the energy-dependent collision strengths (see Fig. 7) over a Maxwellian distribution function. The choice of specifically these two levels is motivated by the fact that their associated satellite lines show a promising polarization effect (see Table I and Fig. 8) that could potentially be undermined by elastic collisions.

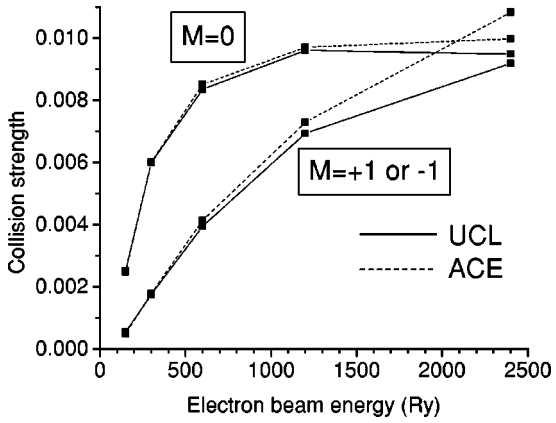

FIG. 6. Comparison of magnetic-sublevel collisional excitation data calculated by UCL and ACE for $1s\ 2s\ ^1S_0,\ M=0 \rightarrow 2s\ 2p\ ^1P_1,\ M=0$ and 1.

Depolarizing effects of thermal electrons are included via isotropic rates of direct (excitation) and inverse (deexcitation) atomic processes linked by detailed balancing. For a given transition between magnetic sublevels of two J levels J_i and J_f, we first calculate the level-to-level collisional rate $R(J_i \rightarrow J_f)$. Then, we "split" the rate evenly among the con-

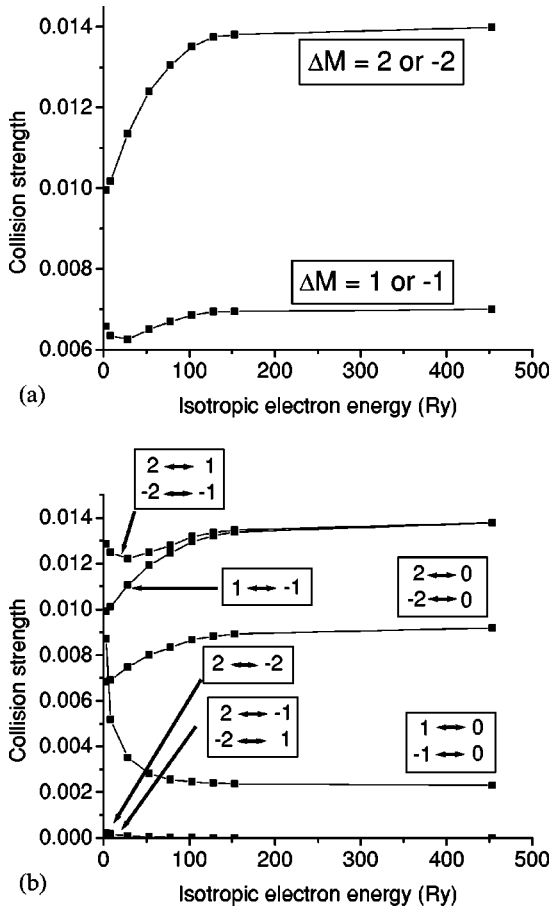

FIG. 7. Elastic scattering data for magnetic sublevels of (a) $2s\ 2p\ ^1P_1$ and (b) $2p^2\ ^1D_2$.

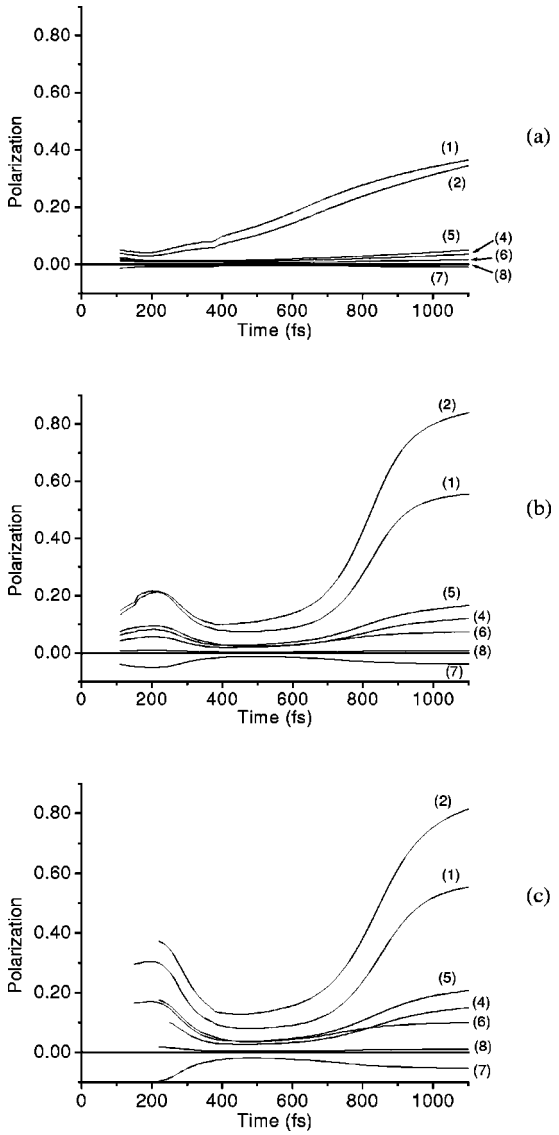

FIG. 8. X-ray satellite lines time-dependent polarization degrees for the (a), (b), and (c) time histories shown in Fig. 3. $I=2\times10^{16}$ W cm^{-2} and $\alpha=0.2$. The numeric key corresponds to the labels indicated in Table I.

stituent sublevel transitions J_iM_i and J_fM_f according to,

$$R(J_iM_i \rightarrow J_fM_f) = \frac{R(J_i \rightarrow J_f)}{2J_f+1}. \quad (4)$$

These sublevel rates are therefore isotropic (i.e., independent of M) in our model. This formula is consistent with J-level kinetics in isotropic plasmas and, in addition, it models the effects of thermal electrons on sublevel kinetics that tend to equalize populations within individual J levels. The formula strictly holds only in isotropic plasmas ($\alpha=0$) but remains a good approximation in case of small alignments, which we do observe during the time interval in plasma evolution when the thermal electrons are most effective.

Polarization-dependent total line intensities are then combined with Voigt line shapes that take into account the effects of natural and Doppler broadening to produce polarization-dependent spectra. For electron densities of order 1×10^{22} cm^{-3} (and larger) Stark broadening effects due to plasma microfields become important in these satellite transitions line shapes. Since the effect of Stark broadening is not currently included in the model, this density sets up an upper bound for its validity. On the other hand, at high densities beam-type electrons are expected to thermalize in which case the polarization effect would be lost.

III. RESULTS

Single-cell electron temperature and density time histories calculated by FILM, beamlike electron distribution functions time histories computed by EUTERPE, and time histories of He- and H-like Si ground-state populations generated by M3R are used to calculate time-dependent magnetic-sublevel populations with POLAR. Then, polarized line intensities (observed at 90° with respect to the quantization axis), degrees of polarization, and time-resolved and time-integrated polarization-dependent synthetic line spectra are computed. The single-cell time histories computed by FILM can also be used to study the dynamics of silicon tracer layers buried in targets made out of other materials, for the sake of recording a silicon polarization signal. In addition, tracer layers of sufficiently small thickness (e.g., submicron) could also be used to minimize space gradients and opacity effects, and thus simplify the interpretation of the spectra. As previously mentioned, α is a constant parameter in these model calculations. To test the consistency of the model, values of α in the $0-0.4$ range were used with the expected results that the polarization effect vanishes for $\alpha=0$ and gradually increases for $\alpha>0$. Here, we illustrate results for the case $\alpha=0.2$, which is estimated to be a reasonable value for the conditions used in these simulations [16]. In an actual application to data analysis, a sensitivity study with respect to the parameter α should be performed. We also emphasize that the details of the electron distribution function are input to our model calculations, and thus calculations could also be done using electron distribution functions obtained from another electron kinetics model and/or code.

Degrees of polarization time histories for the single-cell time histories of Fig. 3 are shown in Fig. 8. The two singlet lines develop significant polarization while the triplet lines remain essentially unpolarized. These time histories provide important information for studying the formation of polarization-dependent line spectra. In general, the atomic kinetics of every cell goes through a strong and fast ionization followed by a slower recombination. The polarization tends to be higher later in time during the recombination phase when the depolarizing effect of the thermal electrons is less important. High peak temperatures in cells closer to the surface also keep the polarization in the outermost cells low around the time of the laser pulse peak. One of the demonstrations of the complexities of the collisional-radiative magnetic sublevel atomic kinetics is the exchange of roles between the two singlet lines ($2s\ 2p\ ^1P_1 \rightarrow 1s\ 2s\ ^1S_0$) and ($2p^2\ ^1D_2 \rightarrow 1s\ 2p\ ^1P_1$) as leading polarization markers depending on the distance from target surface. Electron capture

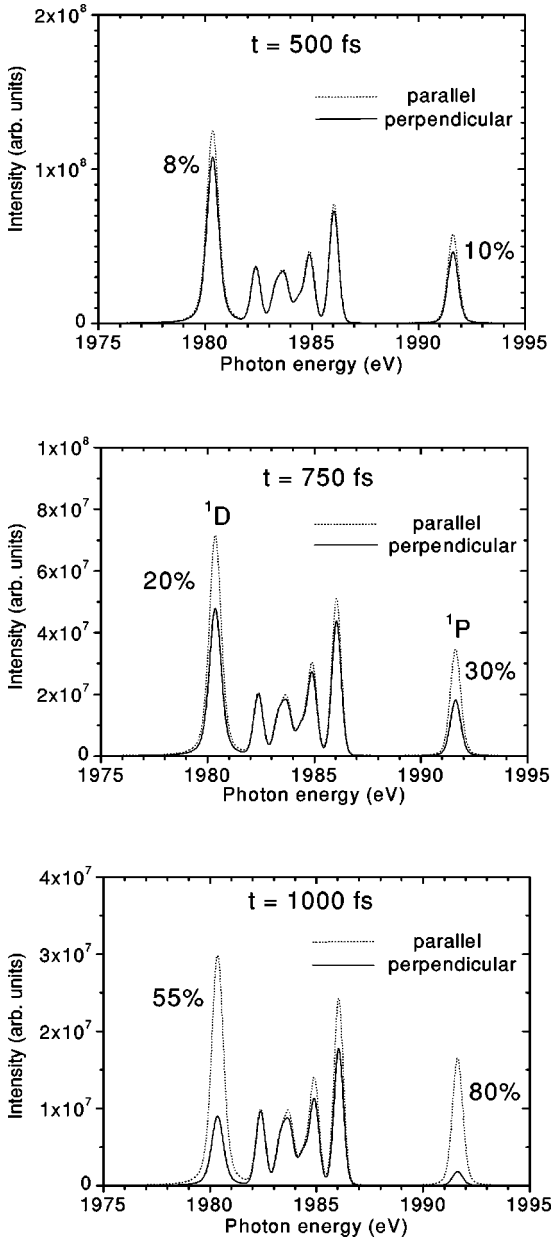

FIG. 9. Parallel and perpendicular polarization-dependent spectra for several instants of time for time history (b) in Fig. 3. $I=2\times10^{16}$ W cm^{-2} and $\alpha=0.2$. The degrees of polarization of the two singlet lines are indicated in the figure.

tends to be more effective in aligning the ^1P upper level but as a feeding channel it is less competitive with collisional excitation favoring the more polarized ^1D deeper in the target. Polarization of the ^1P line surpasses that of the ^1D line closer to the surface where the population of H-like ion's ground state becomes larger relative to the populations of excited states in He-like ions, and the importance of electron capture rises accordingly.

In Fig. 9 we present polarization-dependent synthetic spectra calculated at three times for time history (b) of Fig. 3. These spectra feature a collection of triplet lines flanked by two singlet lines: $2p^2\ ^1D_2 \rightarrow 1s\ 2p\ ^1P_1$ at the low-energy end and $2s\ 2p\ ^1P_1 \rightarrow 1s\ 2s\ ^1S_0$ at the high-energy end. In this

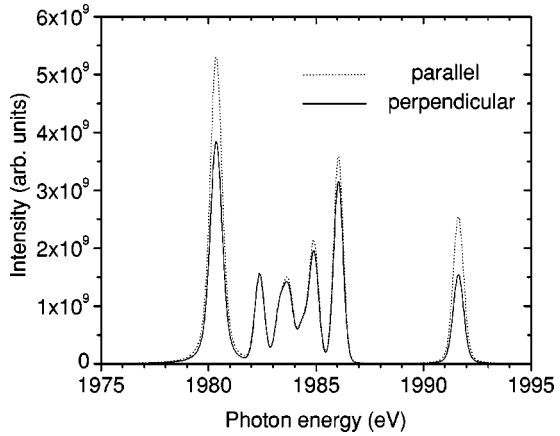

FIG. 10. Time-integrated parallel and perpendicular polarization-dependent spectra for time history (b) in Fig. 3. $I=2\times10^{16}$ W cm^{-2} and $\alpha=0.2$.

figure, polarized lines show nonoverlapping traces associated with parallel and perpendicular intensities while lines with negligible polarization have almost-overlapping parallel and perpendicular traces. According to the corresponding FILM simulation (Fig. 3) the electron number density at these selected time instants has dropped below 10^{22} cm^{-3}. Stark broadening of these Si lines is relatively weak at such conditions; therefore the use of Voigt line shapes including *only* natural and Doppler broadening is justified. As indicated by the polarization degree time histories in Fig. 8, it is the two singlet lines that develop a notable polarization—especially later in time. In Fig. 9 this polarization effect is apparent by the different (i.e., nonoverlapping) intensity distributions pertaining to the two polarization states.

The synthetic spectra in Fig. 9 are time resolved and useful for understanding the formation of polarized line spectra in the plasma. Taking into account early, weakly polarized emissions into a time-integrated synthetic spectra can reduce the polarization effect. The outcome can also be complicated by Stark broadening associated with higher electron number densities early in time. However, this early emission is weak and thus does not change the qualitative appearance of the polarization-dependent synthetic spectra and the reduction of polarization (due to time integration) is modest. Figure 10 shows the time-integrated polarized line spectra for time history (b) of Fig. 3.

We now discuss the dependence of polarized line emission properties on the intensity of the driving laser and the beamlike electron fraction α. The intensities that we considered were 2×10^{16}, 5×10^{16}, 1×10^{17}, and 5×10^{17} W/cm^2. Closer to the surface the total line intensities increase up to an order of magnitude over this range of laser intensities. Deeper in the target line intensities also increase with the laser intensity, although by a smaller amount. The ^1D line remains the strongest line for all laser intensities. We also observe a shift of the emission peak towards earlier times when a stronger laser pulse is used. While the line intensity time histories peak around 500 fs for the 2×10^{16} W/cm^2 laser intensity, the peak of line emission is reached at approximately 300 fs in the 5×10^{17} W/cm^2 laser intensity case. Significant line emission turns on earlier as well; while

TABLE IV. Time-integrated polarization degree of the $2p^2\ ^1D_2-1s\ 2p\ ^1P_1$ line as a function of laser intensity and beamlike electron fraction α.

I(W cm^{-2})	$\alpha=0.1$	$\alpha=0.2$	$\alpha=0.3$	$\alpha=0.4$
2×10^{16}	0.08	0.16	0.22	0.26
5×10^{16}	0.05	0.10	0.14	0.19
1×10^{17}	0.04	0.07	0.11	0.15
5×10^{17}	0.02	0.04	0.06	0.09

the lines begin to "light up" at approximately around 300 fs for the case of 2×10^{16} W/cm^{-2} laser intensity, in the 5×10^{17} W/cm^{-2} case noticeable emissions appear as early as 100 fs. This effect could be explained by a faster rate of plasma ionization associated with higher laser intensities, which then begins to populate the upper levels of the He-like satellite transitions earlier in time. In regard to line polarization we observe a generally decreasing trend for maximum polarization values with increasing laser intensity and for a constant value of α. This effect is most apparent in the case of the two singlet lines. Higher laser intensities produce thermal electrons that are more energetic and also increase the high-energy tail of the beam distribution. In the case of He-like Si satellite lines with excitation thresholds and electron capture resonance energies of about 2 keV, this "energy boost" effectively increases the number of thermal electrons that can drive population into $2l\,2l'$ levels via inner-shell collisional excitation and resonant electron capture processes. This trend increases the role of the thermal electrons in sublevel kinetics, which works against polarization. The same effect, however, moves more of the alignment-creating beam electrons (energies of several keV) even farther from this 2 keV threshold, thus decreasing their competitiveness against the thermal portion of the electron pool. Since the polarization degree is the result of the competing effects of beam (alignment-creating) and thermal (alignment-destroying) electrons, the net result is therefore a gradual reduction of the polarization effect with increasing laser intensity and for a constant α. Thus, for these He-like Si satellite lines we have found that they show a significant polarization effect at laser intensities of 2×10^{16} W cm^{-2} and 5×10^{16} W cm^{-2}, but the polarization becomes weaker at higher laser intensities. For laser intensities above 5×10^{16} W cm^{-2} however, a significant polarization effect in these same line transitions could be expected in an element of larger atomic number (and corresponding threshold energies).

On the other hand, if we keep the laser intensity constant, the polarization degree P will increase for increasing α. To illustrate the sensitivity of the polarization to both free parameters (laser intensity and beam-electron fraction α) Tables IV and V display time-integrated polarization degrees of the two singlet lines for the same fluid element of Figs. 9 and 10. Surface plots and contour lines associated with these tables are shown in Fig. 11. It can be seen that if (as expected) the fraction of beamlike electrons α increases with

TABLE V. Same as in Table IV but for the $2s\ 2p^1P_1-1s\ 2s^1S_0$ line.

I(W cm^{-2})	$\alpha=0.1$	$\alpha=0.2$	$\alpha=0.3$	$\alpha=0.4$
2×10^{16}	0.13	0.25	0.33	0.39
5×10^{16}	0.08	0.16	0.23	0.28
1×10^{17}	0.05	0.11	0.17	0.23
5×10^{17}	0.03	0.07	0.11	0.14

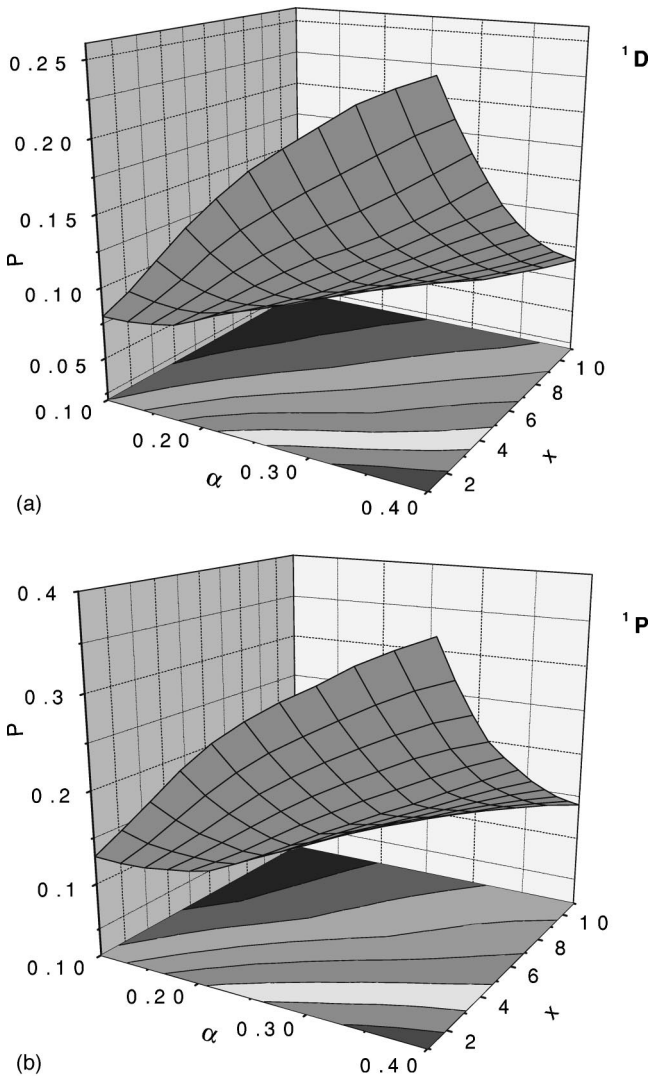

FIG. 11. Surface plots and contour lines associated with the time-integrated polarization degrees shown in Tables IV (a) and V (b); $X=a\log(I/I_0)$, where $a=7.1534$ and $I_0=1.45\times10^{16}$ W cm^{-2}. The range of I is from 2×10^{16} W cm^{-2} ($X=1$) to 5×10^{17} W cm^{-2} ($X=11$).

the laser intensity I, the polarization effect on the singlet lines can also increase. The details will depend on the characteristics of the electron distribution function.

Other potentially depolarizing effects include electron-ion and ion-ion elastic scattering since, when driven by electrons (or ions) characterized by a Maxwellian distribution, they can mix the population of magnetic sublevels associated with a given fine structure energy level and thus destroy the alignment. To address the first effect on the two singlet lines that show polarization, electron-ion elastic scattering cross sections were calculated using the UCL/JAJOM codes of Refs. [5,25], and used to calculate corresponding rates which were then explicitly included in the magnetic sublevel atomic kinetics calculation (i.e., POLAR). Only the Maxwellian part of the electron distribution function associated with the pool of thermal (cold) electrons was used to calculate these rates since the beamlike electrons in the plasma are too energetic to efficiently drive elastic scattering. The effect of electron-ion elastic scattering was found to be negligible in our cases of interest. The influence of ion-ion elastic collisions is also estimated to be negligible based on calculations of ion-dynamics line broadening which result in line widths that are an order of magnitude smaller than those due to electron broadening from elastic collisions.

IV. SUMMARY AND CONCLUSIONS

In order to calculate the characteristics of polarized line emissions we have developed a formalism based on a collisional-radiative atomic kinetics model of magnetic sublevels and the properties of multipole radiation fields. The main emphasis is on the modeling of the atomic kinetics of magnetic sublevels. A parametric model of the electron distribution is used to drive the atomic kinetics calculation. However, we emphasize that the electron distribution function is an input and thus electron kinetics codes that compute electron distribution functions which self-consistently include both thermal and directional electron can be used as well.

We have applied this technique to study polarized x-ray $2l\,2l' \rightarrow 1s\,2l$ satellite line emissions from laser produced silicon plasmas taking into account hydrodynamics, and electron and atomic kinetics effects. We calculated synthetic polarization-dependent spectra - both resolved and integrated in time. We have identified two singlet lines $2p^2\ ^1D_2 \rightarrow 1s\,2p\ ^1P_1$ and $2s\,2p\ ^1P_1 \rightarrow 1s\,2s\ ^1S_0$ to be primary candidates to produce strong polarization effects and therefore serve as polarization markers of plasma anisotropy. On the other hand, the triplet lines ($2p^2\ ^3P_1 \rightarrow 1s\,2p\ ^3P_{0,1,2}$ and $2s\,2p\ ^3P_{0,1,2} \rightarrow 1s\,2s\ ^3S_1$) develop very little polarization and therefore can serve as unpolarized reference lines. We note that the depolarizing effect of elastic scattering due to electron-ion and ion-ion collisions was checked and found to be negligible for the plasma conditions considered here. The model discussed in this paper is general in the sense that it can also be applied to other elements and line transitions.

The study of the laser intensity dependence of polarized He-like Si satellite line spectra reveals that at high laser intensities ($>5\times10^{16}$ W cm^{-2}) the beam-type electrons become too energetic and gradually less efficient to create alignment through collisional excitation or electron capture. However, a higher-Z element will have larger excitation and resonance energies that makes the same line spectra likely to be a useful polarization marker at higher laser intensities.

ACKNOWLEDGMENTS

This work was supported by LLNL Contract Nos. B336460 and B503614, NATO Grant No. CRG 971588, and the UCCSN.

[1] F. Walden, H.-J. Kunze, A. Petroyan, A. Urnov, and J. Dubau, Phys. Rev. E **59**, 3562 (1999).
[2] T. Fujimoto and S. Kazantsev, Plasma Phys. Controlled Fusion **39**, 1267 (1997).
[3] A. S. Shlyaptseva, A. M. Urnov, and A. V. Vinogradov, P. N. Lebedev Phys. Inst. Report No.194 (unpublished).
[4] A. S. Shlyaptseva, R. C. Mancini, P. Neill, P. Beiersdorfer, J. R. Crespo Lopez-Urrutia, and K. Widmann, Phys. Rev. A **57**, 888 (1998).
[5] M. K. Inal and J. Dubau, J. Phys. B **20**, 4221 (1987).
[6] P. Beiersdorfer, D. A. Vogel, K. J. Reed, V. Decaux, J. H. Scofield, K. Widmann, G. Hölzer, E. Förster, O. Wehrham, D. W. Savin, and L. Schweikhard, Phys. Rev. A **53**, 3974 (1996).
[7] S. Fineschi and E. L. Degl'Innocenti, Astrophys. J. **392**, 337 (1992).
[8] P. Hakel, Ph.D. dissertation, University of Nevada, Reno, 2001.
[9] P. Hakel, R. C. Mancini, J. C. Gauthier, E. Minguez, J. Dubau, and M. Cornille, Rev. Sci. Instrum. **72**, 1245 (2001).
[10] A. S. Shlyaptseva, R. C. Mancini, P. Neill, and P. Beiersdorfer, J. Phys. B **32**, 1041 (1999).
[11] J. C. Kieffer, J. P. Matte, H. Pépin, M. Chaker, Y. Beaudoin, T. W. Johnston, C. Y. Chien, S. Coe, G. Morou, and J. Dubau, Phys. Rev. Lett. **68**, 480 (1992).
[12] J. C. Kieffer, J. P. Matte, M. Chaker, Y. Beaudoin, C. Y. Chien, S. Coe, G. Morou, J. Dubau, and M. K. Inal, Phys. Rev. E **48**, 4648 (1993).
[13] M. K. Inal and J. Dubau, Phys. Rev. A **47**, 4794 (1993).
[14] U. Teubner, P. Gibbon, E. Förster, F. Falliès, P. Audebert, J.-P. Geindre, and J.-C. Gauthier, Phys. Plasmas **3**, 2679 (1996).
[15] S. P. Lyon and J. D. Johnson, Los Alamos National Laboratory Report No. LA-CP-98-100, 1998 (unpublished).
[16] A. Rousse, P. Audebert, J. P. Geindre, F. Falliès, J. C. Gauthier, A. Mysyrowicz, G. Grillon, and A. Antonetti Phys. Rev. E **50**, 2200 (1994).
[17] G. Bonnaud and G. Reisse, Nucl. Fusion **26**, 633 (1986); E. Lefebvre, Ph.D. thesis, Université de Paris XI, Orsay, 1996.
[18] R. C. Mancini and E. Mínguez, First International NLTE Atomic Kinetics Workshop, Gaithersburg, MD, 1996 (unpublished); see also R. W. Lee, J. K. Nash, and Y. Ralchenko, J.

Quant. Spectrosc. Radiat. Transf. **58**, 737 (1997).
[19] R. D. Cowan, *The Theory of Atomic Structure and Spectra* (University of California Press, Berkeley, 1981).
[20] B. W. Shore and D. H. Menzel, *Principles of Atomic Spectra* (Wiley, New York, 1968).
[21] E. Takács, E. S. Meyer, J. D. Gillaspy, J. R. Roberts, C. T. Chantler, L. T. Hudson, R. D. Deslattes, C. M. Brown, J. M. Laming, J. Dubau, and M. K. Inal, Phys. Rev. A **54**, 1342 (1996).
[22] J. Abdallah, Jr., R. E .H. Clark, and R. D. Cowan, Los Alamos National Laboratory Report No. LA-11436-M, Vol. I, 1988 (unpublished).
[23] B. J. Archer, R. E. H. Clark, C. J. Fontes, and H. L. Zhang, Los Alamos National Laboratory Report No. LA-UR-02-1526, 2002 (unpublished).
[24] R. E. H. Clark, J. Abdallah, Jr., G. Csanak, J. B. Mann, and R. D. Cowan, Los Alamos National Laboratory Report No. LA-11436-M, Vol. II, 1988 (unpublished).
[25] W. Eissner, Comput. Phys. Commun. **114**, 295 (1998); H. E. Saraph, *ibid.* **15**, 247 (1978).